In situ 3D observations of capillary-driven flows in parallel arrangements of rigid fibres using X-ray microtomography

Chiara Balbinot, Florian Martoïa, Pierre J.J. Dumont, Laurent Orgéas, Jean-Francis Bloch, Sabine Rolland Du Roscoat, Elodie Boller, Frédéric Flin, Pauline Carion, Pierre Latil

In situ 3D observations of capillary-driven flows in parallel arrangements of rigid fibres using X-ray microtomography

C. Balbinot[1,2], F. Martoïa[1*], P.J.J. Dumont[1], L. Orgéas[2], J.-F. Bloch[2], S. Rolland du Roscoat[2], E. Boller[3], F. Flin[4], P. Carion[5], P. Latil[5,2]

[1]*Univ. Lyon, INSA-Lyon, CNRS, LaMCoS, UMR5259, 69621 Villeurbanne, France*
[2]*Univ. Grenoble Alpes, CNRS, Grenoble INP, 3SR Lab, F-38000 Grenoble, France*
[3]*ESRF – The European Synchrotron, Grenoble, F-38043 Cedex 9, France*
[4]*Univ. Grenoble Alpes, Université de Toulouse, Météo-France, CNRS, CNRM, Centre d'Études de la Neige, F-38000 Grenoble, France*
[5]*Univ. Grenoble Alpes, CNRS, Grenoble INP, Agefpi, LGP2, F-38000 Grenoble, France*

*Corresponding author's email: florian.martoia@insa-lyon.fr

Abstract – *Capillary-driven impregnation phenomena occurring in fibre bundles during the processing of composite materials are complex and still not fully understood. Hence, synchrotron X-ray microtomography was used to characterise the longitudinal propagation of the flow front within a parallel arrangement of rigid fibres. The analysis of 3D images enabled the fluid-air interface curvatures, triple line lengths, and local contact angles to be quantified during wetting and dewetting experiments. The results showed that even in quasi-static situations, local contact angles exhibited significant variations along the fibres. These variations also depended on the wetting/dewetting state. The transverse capillary forces measured at the fibre scale from the analysis of 3D images were shown to be of the same order of magnitude as the longitudinal capillary forces. Local curvatures of the fluid-air interface and the resulting estimate of the average capillary pressure proved the relevance of a mesoscale capillary pressure model adapted for fibre bundles.*

Keywords – *B. Surface tension ; C. Transport Phenomena Analysis ; D. CT Analysis ; Capillary forces.*

1. Introduction

Fibre-reinforced polymer composites are increasingly used to produce structural or multi-functional parts for several industrial domains. High-performance composite parts are usually fabricated using liquid composite moulding (LCM) wet-forming processes [1]. In these processes, an impregnation phase of the fibrous reinforcements is required [1,2]. Impregnation consists in the flow of a liquid polymer matrix through a fibrous reinforcement, i.e. within an anisotropic, deformable, and multiscale porous medium made of more or less ordered networks of fibre bundles or yarns [1,2]. Impregnation usually involves the displacement of a non-wetting fluid (air) by a wetting fluid (fluid polymer). In wet-forming processes, the flow of the fluid polymer is induced by either a pressure gradient applied by an injection system, or capillary forces or a combination of both [1,2].

A poor control of the impregnation phase can lead to the onset of several defects such as porosity that are detrimental for the mechanical properties of the composite parts [3-5]. Several studies have shown that capillary effects can significantly affect the propagation of the polymer-air interface, the geometry of which can become extremely irregular, leading to

the formation of pores at various scales [2,4,6]. Capillary phenomena depend on several parameters related to the fluid surface tension, fibre wettability properties (surface energy), contact angle, architecture of the fibre reinforcements (fibre volume fraction), as well as the directionality of the fluid flow with respect to their anisotropy axes, and fluid front velocity (interplay between capillary and viscous effects). In multiscale fibre reinforcements such as reinforcement fabrics, a poor control of capillary-driven phenomena can lead to large differences between the fluid propagation velocity within and between fibre bundles that often result in extreme distortion phenomena of the flow front [3][5][7][8]. To limit the distortion of the flow front and the formation of pores, it is crucial to finely predict the effects of capillary phenomena on the flow of liquid polymer within fibre bundles, i.e. one-dimension fibrous structures made of quasi parallel fibres [9][10].

The study of the impregnation of fibre bundles was the subject of many research efforts [10-14]. Several experiments based on the Wilhelmy method (initially used to study wettability [15], wetting dynamics [16] and more recently surface energy [17] of individualised fibres) were performed to study longitudinal and transverse capillary-driven flows within fibre bundles [18-19]. These experiments consisted in immersing fibre bundles in a test fluid to draw the fluid upward by capillary forces. Measurement of height rise at various times was then related to the fluid surface tension, contact angle and permeability of the fibre bundles. In addition, the fluid propagation in fibre bundles was studied using magnetic resonance imaging (MRI) measurements [20]. This technique enabled detecting variations in fluid concentration and thus the formation of voids/pores during the impregnation of fibre bundles [21]. X-ray radiography was also used to track the propagation of the fluid within fibre bundles [22]. The 2D information provided by this technique was very useful to better understand how the fluid propagated but did not allow the fluid-air interfaces to be finely observed and described. Recently, several studies used 3D X-ray microtomography images to monitor the infiltration process of industrial fibre bundles [23-25]. These studies revealed the formation of preferential flow channels and important fibre rearrangements associated to variations in the fibre volume fraction. An estimation of the fluid-fibre contact angle was also given through the analysis of the 3D images. However, this parameter was measured only in particular zones using 2D cross sections of the 3D X-ray microtomography images [24,25]. In parallel, several studies that were carried out with granular and porous materials showed that it was possible to measure in 3D several interesting local parameters such as the local contact angles [26-29], local mean curvatures [30-33] of the interfaces between the wetting and non-wetting phases. For that purpose, 3D high-resolution images allowing a good description of the geometry of the solid, fluid phases and interfaces were needed.

In this context, the objective of this study was to follow in 3D the fluid front propagation and distortion that occurred during the capillary-driven impregnation of a model fibre network using similar image analysis procedures than those reported for granular materials [26-33]. Note that to establish a relevant methodology, we have first worked on a simplified fibre network made of ordered and parallel millimetre rigid glass tubes/fibres in order to be able, in future studies, to apply this methodology on industrial fibres or fibre bundles made of disordered flexible fibres with smaller diameters and/or irregular cross sections. This approach allowed mimicking the structure of a real fibre bundle used in composite materials

while enabling high-resolution 3D synchrotron X-ray microtomography images to be acquired. For that purpose, several wetting and dewetting stages of the fibre network were imaged using a specially developed impregnation device that was installed on an X-ray microtomography beamline. Thanks to the good compromise between the tube diameter and the spatial resolution of the 3D images, it was possible using specific image analysis procedures to make quantitative measurements of the variations of the local mean curvatures of the fluid-air interface, local contact angles, and lengths of the triple lines. Then, using this database, we estimated the local capillary pressure and the local transverse and longitudinal capillary forces exerted by the fluid on each tube of the fibre network.

2. Materials and methods

2.1 Model fibre networks and impregnation fluids

In this study, several specimens of a fibre network were fabricated. This fibre network was made of parallel hollow glass tubes (Hirschmann, Eberstadt Germany) with an external radius $r_e = 0.75$ mm and an internal radius $r_i = 0.50$ mm. The tubes had a length $L = 16$ mm and were sealed at their top extremity with an epoxy glue to prevent the rising of the liquid inside the tubes. The network was composed of ten tubes arranged in a triangular geometry (Figure 1a,b). The centrelines of each tube were spaced 2 mm apart from each other to form isoscele triangles. The top extremities of the tubes were fixed in a disk made of a plastic resin. To clean the surface of the tubes, the fibre networks were plunged for 1 min inside an ultrasonic bath that was filled with acetone (ACS reagent, Sigma Aldrich).

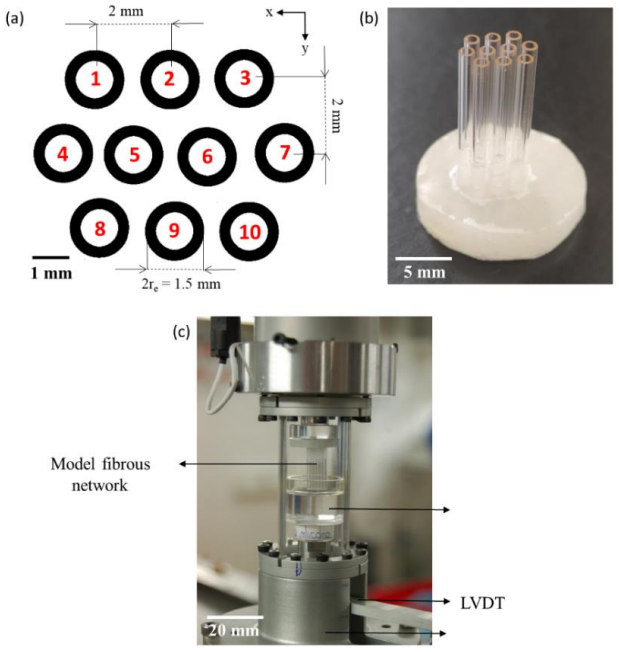

Figure 1. *(a) Scheme of the geometry of the fibre network composed of ten tubes arranged with a triangular geometry. A reference number was attributed to each tube of the fibre network. (b) Photograph of a specimen of fibre network that shows the tube arrangement fixed in the plastic part. (c) Photograph of the micro impregnation device.*

Two Newtonian fluids with controlled rheological and surface tension properties, namely demineralised water and a silicone oil (47V1000 - 80026, Chimie-Plus Laboratoires), were used for the impregnation experiments of the aforementioned fibre network. The shear viscosities η, densities ρ and surface tensions γ_{lv} as well as the tube/fluid static contact angles θ_s of these fluids are given in Table 1. Regardless of the fluid, the static contact angle θ_s was less than 90°, showing that the tube surface can be wetted by both types of fluids.

The Bond number B_o was estimated as r_e^2/λ_c^2 (where $\lambda_c = \sqrt{\frac{\gamma_{lv}}{\rho g}}$ is the capillary length) for the impregnation experiments of the fibre network. $B_o = 0.25$ and $B_o = 0.08$ for the silicone oil and demineralised water, respectively, which shows that the capillary effects were predominant compared to the gravity effects, i.e., fluid menisci are formed around the tubes of the fibre network. It is also important to note that the mean separation distance $2\bar{d}$ between adjacent tubes of the fibre network shown in Figure 1a, was chosen to have $\bar{d}/\lambda_c$ close to 1 for both types of fluids. This separation distance $2\bar{d}$ enables a capillary-driven rising of the fluids within the fibre network.

Table 1. *Properties of the two fluids used for the impregnation experiments. These properties were measured at a temperature $T = 23°C$. The static tube/fluid contact angle θ_s was measured by plunging a single glass tube in the considered fluid using a Krüss tensiometer and applying a correction for the buoyancy force [15]. Note also that the tensiometer was equipped with an optical visualisation setup similar to that described in [16], thus allowing the 2D observation of the static tube/fluid contact angle. The static tube/fluid contact angles θ_s deduced from the Wilhelmy method were close to those estimated from the acquired 2D images.*

Fluid	Surface tension γ_{lv} (mN m^{-1})	Static tube/fluid contact angle θ_s (°)	Shear viscosity η (mPa s)	Density ρ (g cm^{-3})
Demineralised water	72.8 ± 0.1	47 ± 5	1	1
Silicone oil	21.1 ± 0.1	20 ± 2	970	0.97

2.2 In situ impregnation experiments and X-ray microtomography conditions

In situ impregnation experiments of the fibre network were performed using a specially designed setup, as shown in Figure 1c. The setup was composed of an actuator [34] [35] that allowed moving vertically, upwards or downwards, a PMMA reservoir (inner diameter = 18 mm) fixed on it and filled with the impregnation fluid. The vertical position of the reservoir was controlled using a high precision linear variable differential transformer (LVDT) with an accuracy of ± 0.02 mm. The fibre network was fastened on the upper part of the impregnation device. The fibre network and the reservoir were placed inside a transparent cylindrical part made of PMMA fastened to the frame of the actuator. The impregnation device was installed on the rotation stage of a synchrotron X-ray microtomograph (ID19 beamline, ESRF, Grenoble, France) to perform *in situ* impregnation experiments. They consisted in plunging or withdrawing the fibre network in the fluid,

moving at different heights the level of the fluid reservoir using a low translational velocity $v \approx$ 5 µm/s, while taking 3D images of the experiments

Two types of experiments were performed, namely interrupted and sequentially continuous impregnation scanning conditions. The fibre network impregnated with the silicone oil was scanned using interrupted conditions, *i.e.*, the vertical displacement of the reservoir was interrupted at certain positions and after a resting time $\Delta t > 5$ min, a 3D image was acquired. Six different positions or impregnation steps were investigated, moving upwards or downwards the fluid reservoir. The fibre network impregnated with demineralised water was scanned using sequentially continuous conditions. The scans were done while the fluid reservoir was moving upwards or downwards. Six different impregnation steps were studied. During the motion needed to reach every position, a sequence of ten 3D images, corresponding to a total scanning time of approximately 20 s, was taken, thereby allowing *in situ* 3D observations of the impregnation phenomena occurring within the fibre network. To acquire 3D X-ray microtomography images of these experiments, the following imaging conditions were used. The X-ray energy and the number of radiographs (dimensions of the images: 1584×1584 pixels) were set to 36.6 keV and 800, respectively. The exposure time of each radiograph was 2 ms and the scan duration less than 2 s. From the radiographs, 3D images with a voxel size of 5.1^3 µm^3 were reconstructed using the so-called Paganin procedure to enhance phase contrast in the images [36]. These ultrafast acquisition conditions and image resolution allowed obtaining an accurate representation of the tubes and the fluid front propagation, while having a sufficiently large field of view. Note that the acquisition parameters, and in particular the image spatial and time resolution, could be adjusted in future studies to analyse impregnation phenomena occurring in industrial fibrous media made of disordered compliant fibres with smaller diameters and faster impregnation characteristic times [35][37].
The capillary number C_a related to the impregnation experiments was estimated as $\frac{\eta v}{\gamma_{lv}}$. For the experiments performed with silicone oil (resp. demineralised water) $C_a \approx 2 \times 10^{-4}$ (resp. $C_a \approx 8 \times 10^{-8}$), thus showing that in both cases the surface tension effects were largely predominant compared to the viscous effects. Hence, both imaging conditions can be considered as delivering 3D images of a sequence of quasi-static states of the flow front propagation governed by the capillary effects.

2.3 3D image analysis

Identification of the triple lines – After proper segmentation of the 3D images using Fiji [37] as described in Figure 1 in S1, we developped a procedure to identify the triple lines that formed on the external surface of the tubes between the fluid, tube and air phases. The identification was applied on each tube of the fibre network and consisted in several steps. For that purpose, a "crop" operation was performed on the full 3D images to obtain sub-volumes centred on the tube axes (dimensions of the sub-volumes: 400×400×900 voxels). Then, the inner cavity of each tube was "filled" using the "Fill holes" function of Fiji [38] (see Figure 2). 3D dilation operations were then performed for each phase of the sub-volumes using the plugin Analysis 3D. Figure 2b illustrates this operation, showing in red the phase

that was subjected to 3D dilation and cross-sections of the resulting 3D images for the three phases. These 3D images were then intersected using the Image calculator function, which allowed keeping only the common voxels of the three phases (Figure 2c) and then skeletonized to obtain the voxels belonging to the triple line (Figure 2d).

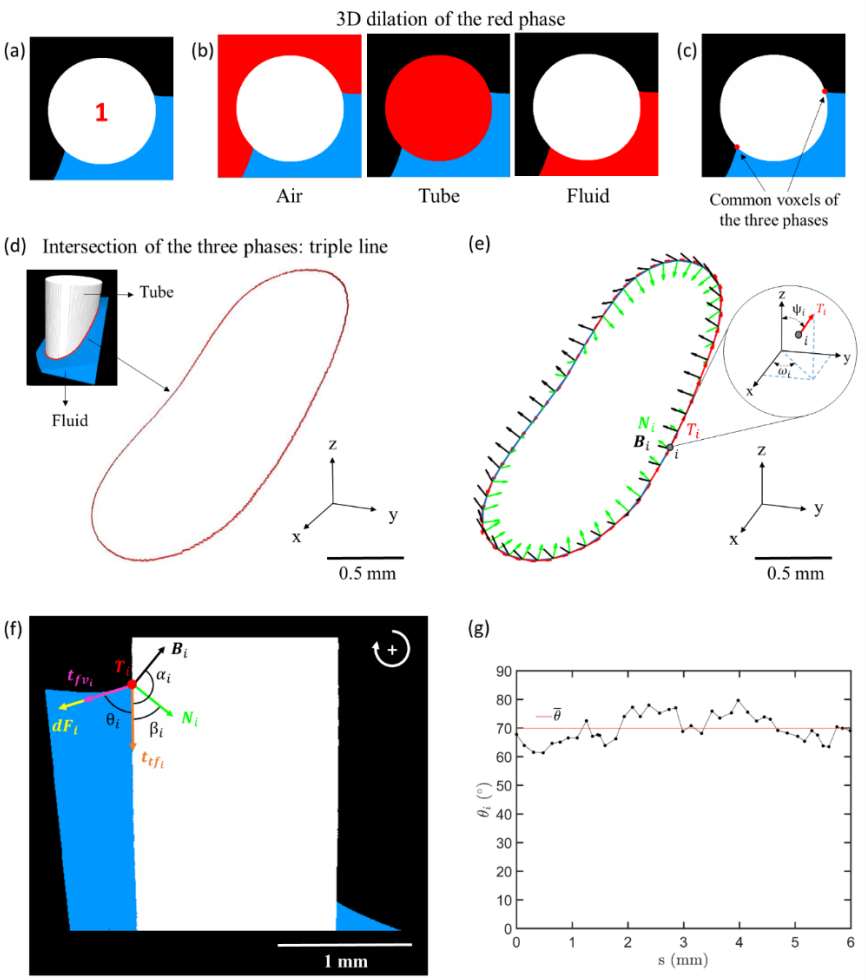

Figure 2. *Procedure used to identify the triple lines and to measure the local contact angles. (a) View of a horizontal cross section of a trinarised 3D sub-volume centred on the axis tube n°1 of a fibre network. (b) Same images showing the results of the 3D dilation operations that were performed on the air, tube and fluid phases. (c) Same image as (a) showing in red the voxels belonging to the air, tube and fluid phases and corresponding to voxels belonging to the triple line. (d) 3D view of the corresponding triple line. (e) Smoothed linear parametric representation of the triple line with the local Frenet bases* $(\boldsymbol{T}_i, \boldsymbol{N}_i, \boldsymbol{B}_i)$ *associated to each elementary discretisation segment* i*. (f) View of a cross section in a* $(\boldsymbol{N}_i, \boldsymbol{B}_i)$ *plane of the 3D sub-volume and associated tangent vectors to the tube-fluid and fluid-air interfaces as well as the local contact angles* θ_i*. The arrow shows that a clock-wise positive measurement of angles was chosen by convention. (g) Evolution of the local contact angle* θ_i *along the curvilinear abscissa* s *of the triple line.*

Measurements of the triple line lengths and local contact angles – The measurements of the length of the triple line and the local contact angles along it were performed with a procedure

we implemented in Matlab [34]. Smoothed closed linear parametric curves of the triple lines with curvilinear abscissa s were fitted using the set of discrete voxels of coordinates (x, y, z) representing the triple lines in the 3D images that were obtained following the procedure described in the previous section. This parametric curve was then discretized into N_s elementary segments i of lengths ds_i with $1 \leq i \leq N_s$. Depending on the considered tube and on the shape of the triple line, N_s could vary from 35 to 60. The lengths l_s of the triple lines were computed as $l_s = \sum_{i=1}^{N_s} ds_i$. It was verified that such discretization gave a good approximation of the lengths of numerically generated circular triple lines. Then, a local Frenet basis was associated to each elementary segment i using the calibrated procedure reported by Latil *et al.* [34]. In this local basis, $\boldsymbol{T}_i$ is the tangent unit vector, $\boldsymbol{N}_i$ is the normal unit vector pointing towards the tube, and $\boldsymbol{B}_i$ the binormal unit vector to the segment i (Figure 2e).

For measuring the N_s local contact angles θ_i along the triple lines, the trinarised 3D images were cut in the $(\boldsymbol{N}_i, \boldsymbol{B}_i)$ planes using the image rotation function of the image processing toolbox of Matlab. For that purpose, the 3D images were successively rotated of an angle ω_i around the z axis and of an angle ψ_i around the y axis of the (x, y, z) frame of the 3D images (Figure 2e). Then the local contact angles θ_i were measured manually as the angle formed between the vector $\boldsymbol{t}_{tf_i}$ tangent to the tube (marked in orange) and the vector tangent to the fluid surface $\boldsymbol{t}_{fv_i}$ (marked in pink), using a ROI of 50×50 pixels centred on the triple points. This procedure was also validated with numerically generated images, exhibiting the same spatial resolution of the X-ray microtomography images and a predefined local contact angle varying from 5° to 90°. To predefine the local angle in the numerically generated images we used a generation process based on the theoretical expression proposed by James (1974) [39] that predicts the equilibrium shape of a meniscus that is formed on the outside of a circular vertical cylinder. The error made following this procedure was shown to be ±3°. Figure 2g shows an example of the evolution of the local contact angle θ_i and its mean value $\bar{\theta}$ along a triple line. Besides, it is important to mention that the aforementioned procedure was performed for each triple line that formed along all the tubes of the fibre network.Mixtures of water and tBuOH resulted in aerogels with smaller pores and yielded smaller crystal sizes depending on the freezing conditions.55 Only the data obtained with the aerogels frozen at -196 °C are presented herein because the samples with tBuOH frozen at -50°C could not be unmolded properly due to mechanical instability, leading to the collapse of the structure. The resulting microstructures are very different from those obtained without tBuOH. For example, the cross section displayed in figure 1.i. shows a lamellar structure of this material with pores of 133 ± 34 µm average length and 33 ± 7 µm average width. Such lamellae were not observed without tBuOH, and the pores appear significantly larger. This structural modification resulted in important changes on both electrical and mechanical properties of the aerogel. Thus, R_{2P}^{1cm} was measured at 18 Ω, *i.e.*, 65 % lower than samples without tBuOH. Similarly to AgNWA fabricated at -50 °C, AgNWA-tBuOH had bigger pores and thicker and presumably denser pore walls, resulting in a higher number of electrical contacts between AgNWs, and therefore a lower electrical resistance. More importantly, both Young's modulus and yield strength were, however, divided by 4 compared to free-tBuOH samples (3.4 ± 0.3 kPa and 0.16 ± 0.02 kPa against 12.0 ± 1.5 kPa, 0.74 ±

0.05 kPa for AgNWA-tBuOH-196 °C and AgNWA-196 °C respectively), which could be detrimental for some applications. Since AgNWA fabricated at 50 °C displayed the best electrical and mechanical properties, the study was then carried out by freezing on the trays at -50 °C, without addition of tBuOH.

Measurements of the capillary forces – Using the cross sections of the rotated 3D images, it was also possible to estimate for each segment i of a given triple line the components in the $(\boldsymbol{N}_i, \boldsymbol{B}_i)$ basis of the local capillary force $\mathrm{d}\boldsymbol{F}_i = \gamma_{lv}\mathrm{d}s_i\boldsymbol{t}_{fv_i}$ exerted by the fluid on a portion of tube as follows:

$$\mathrm{d}F_{i\ B} = \mathrm{d}\boldsymbol{F}_i \cdot \boldsymbol{B}_i = \gamma_{lv}\cos(\theta_i - \alpha_i)\mathrm{d}s_i \quad (1)$$

$$\mathrm{d}F_{i\ N} = \mathrm{d}\boldsymbol{F}_i \cdot \boldsymbol{N}_i = \gamma_{lv}\cos(\theta_i - \beta_i)\mathrm{d}s_i \quad (2)$$

where the angles α_i and β_i are shown in Figure 2f. The overall capillary force $\boldsymbol{F}$ exerted by the fluid on a given tube was obtained by summing all the local capillary forces $\mathrm{d}\boldsymbol{F}_i$. Then, the components F_x, F_y and F_z of the capillary forces were calculated using the coordinates of the $\boldsymbol{N}_i$ and $\boldsymbol{B}_i$ vectors in the (x, y, z) frame of the 3D images. Hence, the intensities of the transverse $F_\perp = \sqrt{F_x^2 + F_y^2}$ and longitudinal $F_\parallel = |F_z|$ capillary forces exerted by the fluid on each tube of the model fibre network were determined.

Measurements of surface curvatures – The local mean curvatures of the interface between the fluid and the air phases were estimated using an approach developed and calibrated by Flin *et al.* [40] [41]. The method is based on the expression of the mean curvature κ at a point P located at the interface between the fluid and the air, which is defined as the divergence of the downward unit normal vector $\boldsymbol{n}(P)$:

$$\kappa(P) = \frac{\boldsymbol{\nabla} \cdot \boldsymbol{n}(P)}{2} \quad (3)$$

The algorithm computes the normal vectors $\boldsymbol{n}(P)$ using the volumetric information related to the gradient in the grey levels of the signed distance map of a binarised 3D image of the fluid phase (see Figure 2a shown in S1). An example of a 3D map of the mean curvature of the fluid-air interface is shown in Figure 2b (S1). A corresponding 2D map of the mean curvature κ is shown in Figure 2c (S1) and was obtained by projecting the 3D map on the (x, y) plane. This 2D map was then smoothed with a coarse graining approach [42]. To check the relevance of the measurements, the algorithm was tested using binarised 3D images of the tubes whose curvature is known. From the mean curvature map, it was then possible to estimate the local capillary pressure P_c using the Laplace-Young equation:

$$P_c = P_v - P_l = 2\ \gamma_{lv}\kappa \quad (4)$$

where $P_v - P_l$ is the pressure difference across the air-fluid interface.

3. Results

3.1 Model fibre networks and impregnation fluids

Figure 3 shows vertical cross sections of the 3D images acquired during the impregnation of the model fibre network with silicone oil or demineralised water.

Impregnation sequence using interrupted scanning conditions – The impregnation experiment that was performed using the silicone oil consisted in a sequence of six impregnation stages. They are denoted A–F in Figure 3a. In image A, the silicone oil was not in contact with the fibre network. The bottom extremities of the tubes were located at a vertical distance of approximately 2 mm of the fluid-air interface, as shown in the position-time graph in the inset of Figure 3a. This image revealed that the fluid-air interface was nearly planar in spite of the rotation of the X-microtomograph stage during scanning. In stage B, the fibre network was immersed in the silicone oil. The extremities of the tubes reached a depth of approximately -0.3 mm measured with respect to the initial position of the fluid-air interface of stage A. In stage C, this depth was -4.2 mm. Then the fluid reservoir was moved downwards in stages D and E until the fluid meniscus that formed between the tubes and the fluid was broken (stage F). Images obtained for stages B and C showed that the fluid rose between the tubes of the fibre network. The fluid reached its maximum height in the centre of the network and the fluid-air interface formed a dome-like shape at the network scale. Note also that the image spatial resolution allows observing the shape of the tube scale menisci that formed where the tubes crossed the fluid-air interface. Besides, as the tubes were sealed at their top extremities, the fluid could not rise inside the tubes. Only a slight meniscus formed at their lower extremities. Images B and C did not reveal any significant changes between the overall shape of the dome that formed within the fibre network apart from its left-hand and right-hand side borders (close to tubes 4 and 7), where a slight difference in the shape of the menisci was noticed. Similar observations could be done for the outer tubes of the fibre network. For the tubes 5 and 6, these observations revealed that the fluid tended to slide on the tube surfaces when the reservoir was lifted up. When the reservoir was pulled down (stages D and E), again the fluid tended to slide on the tube surfaces which induced that the dome-like shape of the fluid-air interface was mostly preserved. However, the shape of the menisci of the outer tubes was affected. These phenomena will be further analysed and quantified in the next subsections by quantifying the local contact angles θ_i and the lengths of the triple lines l_s along all the tubes for stages B and E. In stage F, the reservoir was further pulled down, which resulted in the breakage of the capillary bridge. Finally, a volume of liquid was entrapped within the model fibre network.

Impregnation sequence using sequentially continuous scanning conditions – The impregnation experiment described in this section was performed using demineralised water in a sequence of six impregnation stages (A-F) of the fibre network. For each stage a sequence of ten images (A_i, B_i, C_i... with $i = 1, 2 \ldots 10$) was obtained (1 image every 2 s). Starting from the initial position (stage A_1), where the extremities of the tubes were above the fluid surface, the fluid reservoir was moved upwards and the extremities of the tubes entered in contact

with the fluid (stage A_{10}), as shown in Figure 3b. Then, the reservoir was further moved upwards (stage B) before being gradually withdrawn (stages C-F). Similarly to the previously described impregnation experiment performed with the silicone oil, a dome-like shape of the fluid-air interface was obtained at the network scale. However, the height of the "dome" reached at the centre of the fibre network was lower. Slight height variations of the fluid-air interface were visible in the vertical cross section in Figure 3b. These variations were due to slight vertical misalignments of the tubes of the fibre network used in this experiment. Contrary to what was observed with silicone oil, it is visible from Figure 3b of stage F that the capillary bridge was not broken for a similar withdrawing position of appr. 2 mm.

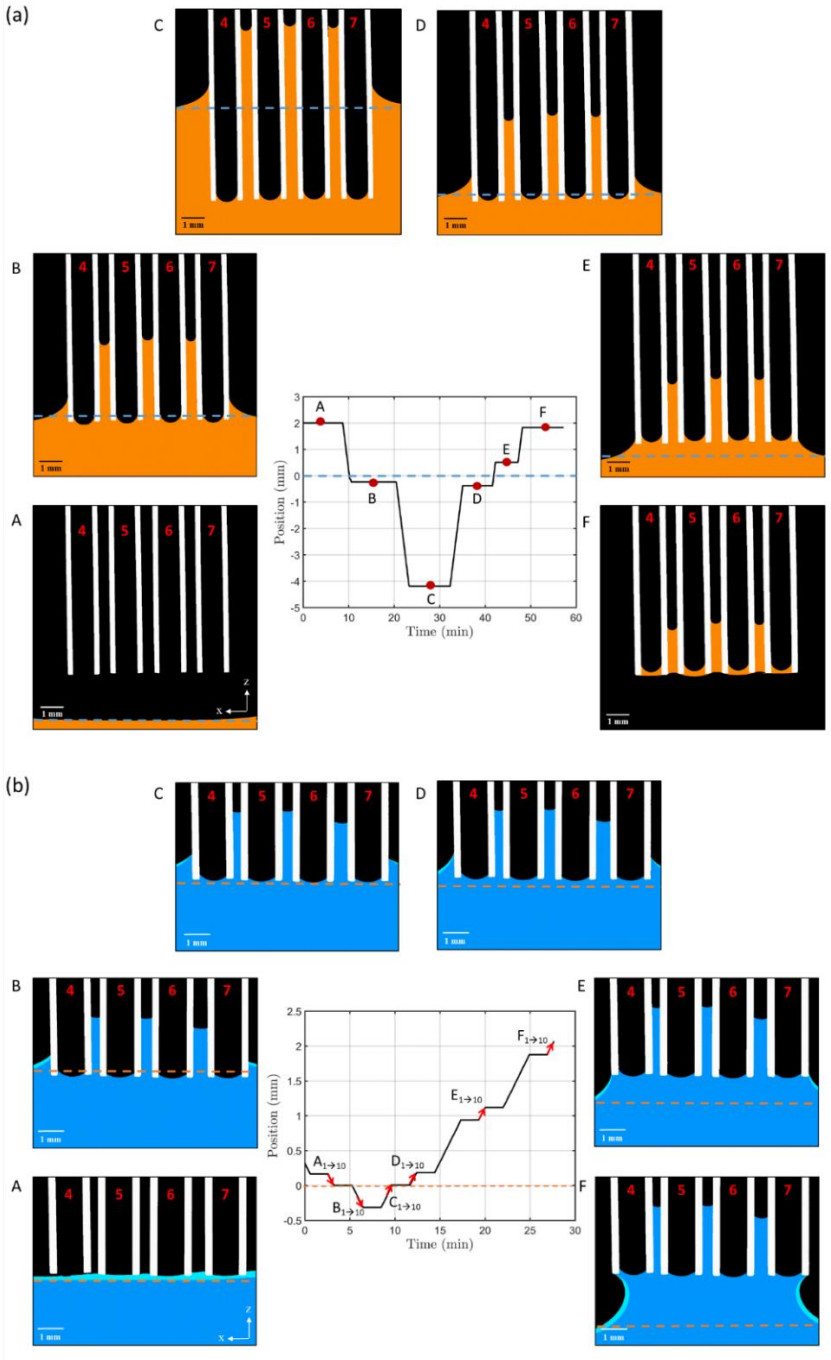

Figure 3. *Vertical cross sections of the 3D images acquired during the impregnation of the fibre network with silicone oil (a) and demineralised water (b). The dashed lines show the initial position of the fluid surface. The tubes are represented in white, the air in black, the silicone oil in orange and the demineralised water in blue. The graphs represent the position of the bottom extremities of the tubes with respect to the initial position of the fluid surface as a function of time. The red arrows in the graph indicate the time intervals when the sequences of 3D images were acquired*

In Figure 3b, the zones of the fluid phase highlighted with a lighter blue were obtained by subtracting the volume of fluid of image 1 (resp. image 10) to image 10 (resp. image 1) for the sequences $A_{1\text{-}10}$ and $B_{1\text{-}10}$ ($C_{1\text{-}10}$, $D_{1\text{-}10}$, $E_{1\text{-}10}$ and $F_{1\text{-}10}$). This allows the evolution of the geometry of the fluid front to be followed live for 20 s. For each stage (from B to F), the vertical cross sections show that the fluid that was entrapped in the centre of the fibre network (around tubes 5 and 6) did not move significantly. On the contrary, the fluid motion could be clearly observed on the edges of the fibre network (tubes 4 and 7 in the vertical cross section of Figure 3b). The vertical cross section of stage B shows that the menisci that formed on the inner tubes 5 and 6 did not exhibit significant geometric changes between images B_1 and B_{10}. In addition, the menisci that formed on the outer tubes of the fibre networks showed slight changes. Thus, the fluid tended to slide on the surfaces of the tubes of the fibre network. The evolution of the menisci will be discussed in detail in the next sections. Stages C-F reveal that the menisci that formed on the inner tubes 5 and 6 were apparently not affected by the withdrawing motion of the reservoir. On the contrary, the menisci that formed on the outer tubes were distorted. The triple line was like anchored on the outer tubes. The positions of the triple points on tubes 4 and 7 in Figure 3b did not change and the local contact angles exhibited a decrease (the values of the local contact angles θ_i will be given in next subsections).

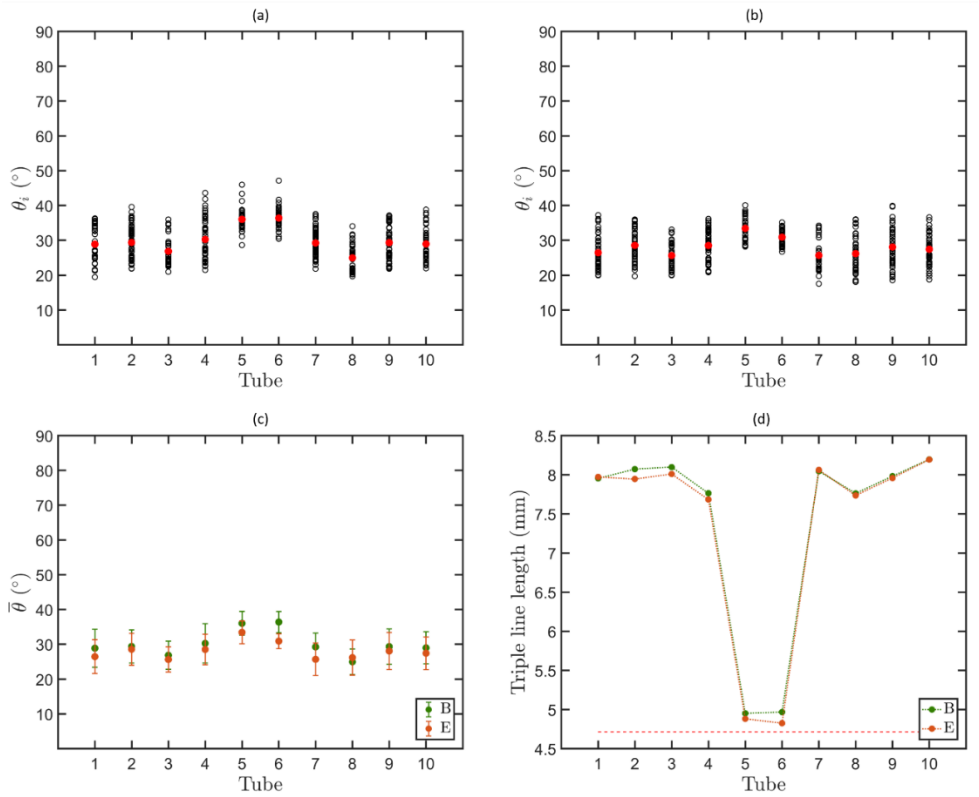

Figure 4. *Local contact angles θ_i measured along the triple lines of all the tubes of the fibre network for stages B (a) and E (b) of the impregnation experiment performed using silicone oil. (c) Corresponding mean values $\bar{\theta}$ and standard deviations for stages B and E. (d) Lengths of the triple lines for all the tubes of the fibre network for stages B and E. The red dashed line represents the length of the perimeter of the cylindrical tubes used to build the fibre network*

3.2 Contact angles and triple line lengths

Interrupted conditions – Figures 4a,b show the evolution of the local contact angles θ_i along the triple lines that formed along all the tubes of the fibre network for stages B and E for the experiments performed with the silicone oil. For these two stages, these figures show that θ_i exhibit a great variation along the triple lines, regardless of the tube. The difference between the maximum and the minimum values was almost 15° for each tube. The dispersion of the values of the local contact angles was higher for the outer tubes whose triple lines were more distorted than for the tubes located at the centre of the fibre network (tubes 5 and 6). A further analysis of the evolution of the local contact angles along the triple lines of all the outer tubes showed that the lowest values of θ_i were obtained for regions of the triple lines that were not located in the vicinity of other tubes.

Figure 4c shows the mean values $\bar{\theta}$ of the local contact angles θ_i for all the tubes of stages B and E, as well as the standard deviation of θ_i. The mean contact angle $\bar{\theta}$ varied for all the tubes. However, it is interesting to notice that the mean contact angles $\bar{\theta}$ of the tubes in symmetry positions (tubes 1, 3, 8, 10 or tubes 2, 9 or tubes 5, 6) were almost equal. The mean value $\bar{\theta}$ of the tubes 5 and 6 at the centre of the fibre network were also slightly higher than those measured for the outer tubes. In stage B, the mean value was 35° for tubes

5 and 6, whereas it was 29° for the outer tubes. In stage E, this difference decreased: the mean value $\bar{\theta}$ of the tubes 5 and 6 was 32°, whereas it was 27° for the outer tubes. This difference shows that the mean contact angles $\bar{\theta}$ tended to decrease with the withdrawing of the reservoir.

Figure 4d shows the lengths of the triple lines for stages B and E. For the tubes 5 and 6, the lengths of the triple lines were almost similar to that of the perimeter of the tube (~4.8 mm). The triple lines of the outer tubes were strongly distorted (see also Figure 2d) and their lengths were much greater (~8 mm). However, there were no significant changes between the lengths measured in stages B and E.

Sequentially continuous conditions – Figure 5a shows the mean contact angles $\bar{\theta}$ measured for stages B_1 and B_{10}, D_1 and D_{10} and their standard deviations for the impregnation experiments performed using demineralised water. As observed previously, the mean contact angle $\bar{\theta}$ also varied for all the tubes. In addition, the mean contact angles $\bar{\theta}$ for stage B_1 were slightly lower than for stage B_{10}. For stages B_1 and B_{10}, $\bar{\theta}_{B_1} = 72°$ and $73°$, respectively. A more pronounced difference could be observed for the outer tubes than the inner ones (5 and 6). The origin of this slight increase might be due to the flattening of the menisci that formed around the tubes when the reservoir was lifted up (or conversely when the fibre network was plunged into the demineralised water).

On the contrary, when the reservoir was withdrawn, the mean contact angle tended to decrease between stages D_1 and D_{10} in a more pronounced manner, i.e., $\bar{\theta}_{D_1} = 63°$ and $\bar{\theta}_{D_{10}} = 58°$. It was also apparent that the standard deviation values were larger for stages D than B, *i.e.*, during the withdrawing of the reservoir. This result is confirmed by the difference between the maximum and the minimum values of the contact angles that was equal to 15° (resp. 45°) for stage B (resp. D).

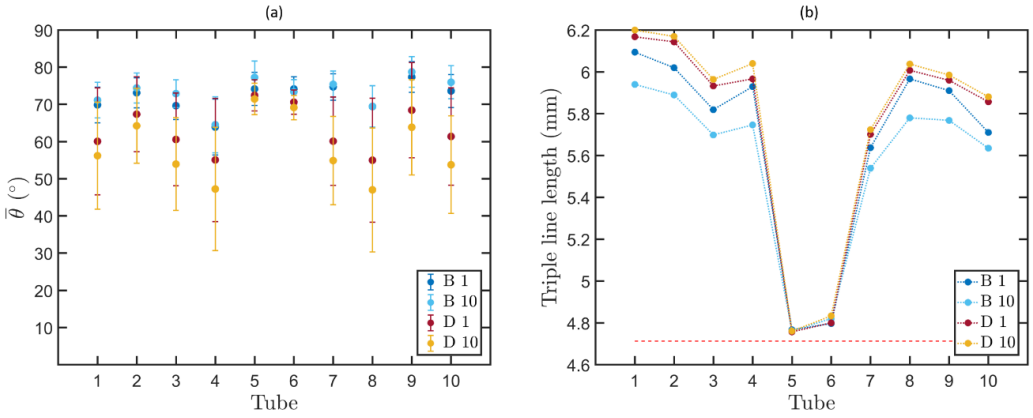

Figure 5. *(a) Mean contact angles $\bar{\theta}$ for all the tubes of the fibre network and stages B_1, B_{10}, D_1 and D_{10} of the impregnation experiment performed using demineralised water. (b) Corresponding lengths of the triple lines.*

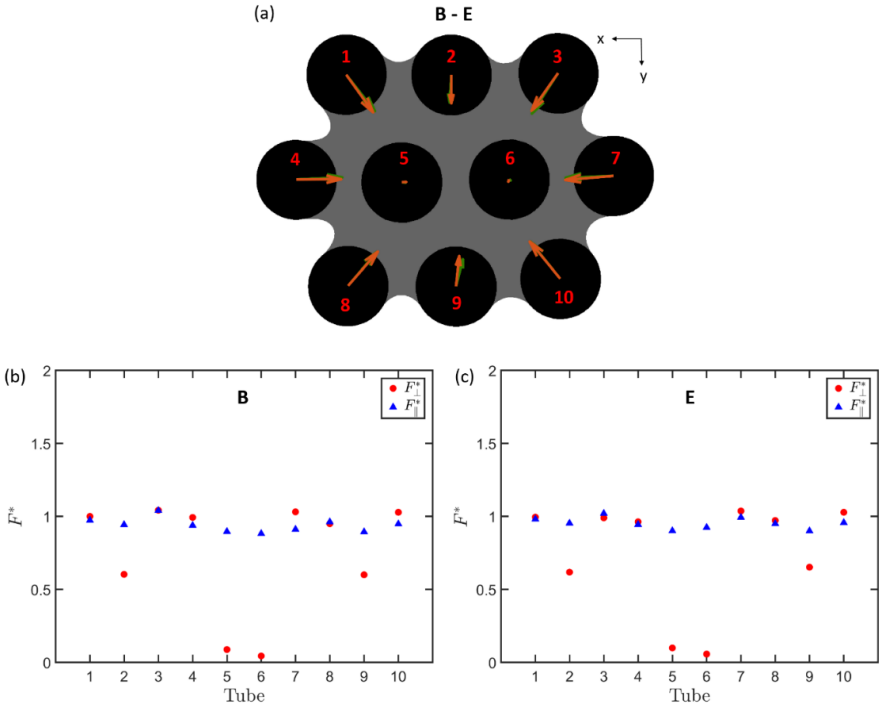

Figure 6. *(a) Cross section of the fibre network showing the transverse capillary force $F_\perp$ exerted by the fluid on each tube (in black) for stages B (green arrows) and E (orange arrows) of the impregnation experiment carried out with the silicone oil. The application points of the forces were placed arbitrarily on the axes of the tubes. The cross section of the fibre network was also chosen arbitrarily (the fluid is grey in the cross section). Graphs showing the dimensionless transverse $F_\perp^*$ and longitudinal $F_\parallel^*$ capillary forces exerted by the fluid on each tube for stages B (b) and E (c).*

Figure 5b shows the variation of the lengths of the triple lines for the same stages. For the inner tubes (5 and 6), no clear differences in the lengths of the triple lines could be observed. This is in accordance with the observations made in subsection 3.1.2: the positions of the fluid-air interface and triple lines at the centre of the fibre network did not vary significantly when the reservoir was moved upwards or downwards. The lengths of the triple lines along the outer tubes tended to decrease when the reservoir was lifted up, as shown for stages B_1 and B_{10}. This could be related to the increase in the position of the fluid-air interface around the fibre network. In contrast, the lengths of the triple lines between stages D_1 and D_{10} increased slightly. In parallel, the mean contact angles $\bar{\theta}$ showed a large decrease, thus confirming the observations made on the vertical cross sections shown in Figure 3b, *i.e.*, the triple lines were like anchored on the tube surface during the withdrawing of the reservoir.

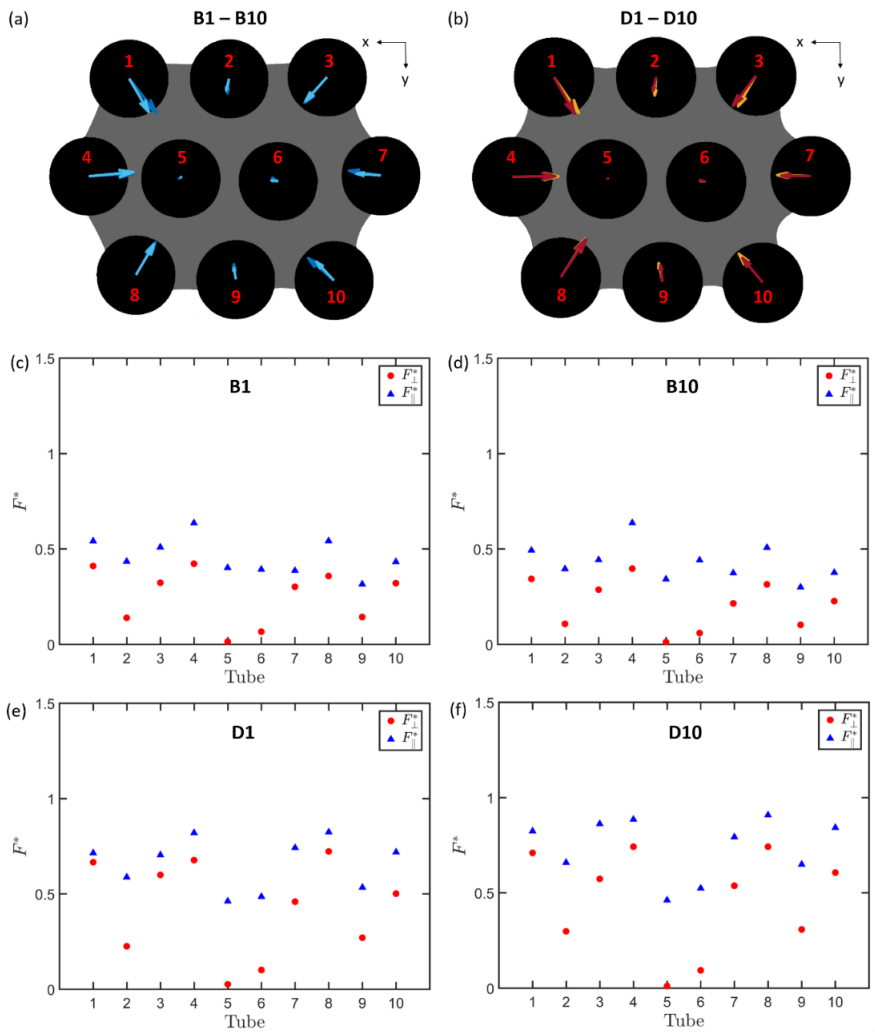

Figure 7. *(a,b) Cross sections of the fibre network showing the transverse capillary force $F_\perp$ exerted by the fluid on each tube (in black) for stages B_1 (dark blue arrows) and B_{10} (pale blue arrows) and D_1 (red arrows) and D_{10} (yellow arrows) of the impregnation experiment carried out with the demineralised water. The application points of the forces were placed arbitrarily on the axes of the tubes. The cross section of the fibre network was also chosen arbitrarily (the fluid is grey in the cross section). Graphs showing the dimensionless transverse $F_\perp^*$ and longitudinal $F_\parallel^*$ capillary forces exerted by the fluid on each tube for stages B_1 (c), B_{10} (d), D_1 (e) and D_{10} (f).*

Capillary forces – The direction and intensity of the transverse capillary force $F_\perp$ exerted on each tube by the fluid are shown in Figure 6a-c and Figure 7a-c for the sample impregnated with the oil for stages B and E, and demineralised water for stages B_1, B_{10}, D_1 and D_{10}, respectively. In addition, the normalised intensities of the transverse $F_\perp^* = F_\perp/(2\pi r_e \gamma_{lv} cos\theta_s)$ and longitudinal $F_\parallel^* = |F_z|/(2\pi r_e \gamma_{lv} cos\theta_s)$ capillary forces measured for each tube are reported in Figure 6b,c and Figure 7d,e for the two impregnation experiments.

Figures 6a and 7a-b show that the transverse forces $F_\perp$ exerted on the inner tubes were negligible. On the contrary, the transverse forces $F_\perp$ exerted on the outer tubes tend to

point towards the centre of the fibre network, regardless of the impregnation stages for both experiments. Slight variations in the directions of $F_\perp$ could be observed between the various impregnation stages. These results were in accordance with the aforementioned variations of the local contact angles and lengths of the triple lines (Figures 4 and 5).

In addition, Figures 6b,c and 7c-f show the dimensionless transverse $F_\perp^*$ and longitudinal $F_\parallel^*$ capillary forces exerted by the fluid on each tube. For the inner tubes (5 and 6), the transverse forces were negligible which is due to the symmetries of the fibre networks, whereas for some of the outer tubes (tubes 1, 3, 4, 7, 8 and 10), both forces were of the same order of magnitude. For tubes 2 and 9, the transverse capillary forces were approximately one half or more lower than the longitudinal forces. Figures 6b,c show that the dimensionless longitudinal capillary forces were approximately equal to 1 (except for tubes 2 and 9). This tends to show that the longitudinal capillary force exerted by the fluid on each tube of the fibre network is close to that obtained for a single tube plunged in the silicone oil with a meniscus that would form a constant contact angle equal to θ_s. As already noticed for the measurements of the mean contact angles, the forces obtained for the experiments performed with the demineralised water showed a higher discrepancy than those measured for the silicone oil. A possible origin of this discrepancy might be a poorer precision in the placement of tubes (e.g. slight inclination or misalignment) in the fibre network used for the experiments performed with the demineralised water. This discrepancy could also be related to a wider diversity of physicochemical interactions between water and the surfaces of the tubes [43].

For the experiments performed using the silicone oil, the comparison of Figures 6b and 6c show that the withdrawing of the fluid reservoir tended to slightly increase the dimensionless longitudinal capillary forces $F_\parallel^*$. This effect was less clear for the dimensionless transverse capillary forces $F_\perp^*$. This increase could be associated to the slight decrease in the mean contact angles as shown in Figure 4c. A similar but more pronounced tendency to the increase in both capillary forces is revealed by comparing Figure 7c,d with Figure 7e,f. More interestingly, the comparison of stages B_1 (resp. D_1) with B_{10} (resp. D_{10}) shows a decrease (resp. an increase) in both capillary forces when the reservoir was moved upwards (resp. downwards). Again, these tendencies have to be related to the aforementioned evolutions of the contact angles and lengths of the triple lines, as shown in Figure 5a,b.

Fluid front curvatures and capillary pressure – Figure 8a shows a 2D map of the mean curvature κ for stage B of the impregnation experiment performed using silicone oil. The mean curvature κ measured in the centre of the fibre network ranged between 0.80 mm^{-1} and 1.20 mm^{-1} (Figure 8a). Consequently, the local capillary pressure P_c in the centre of the model fibre network ranged between approx. 35 and 55 Pa (Figure 8b).In addition, Figure 8c shows that the average capillary pressure $\bar{P}_c$ measured in the centre of the fibre network did not show large variations, regardless of the impregnation stages. This is in accordance with the previous observations related to Figure 3b since the geometry of the dome-like shape of the fluid-air interface did not exhibit significant changes. On the outer edge of the fibre network, the mean curvature κ was lower and ranged between 0.36 mm^{-1} and 0.50 mm^{-1} (Figure 8a). This corresponds to a local capillary pressure P_c that was comprised between 15 Pa and 21 Pa (Figure 8b).

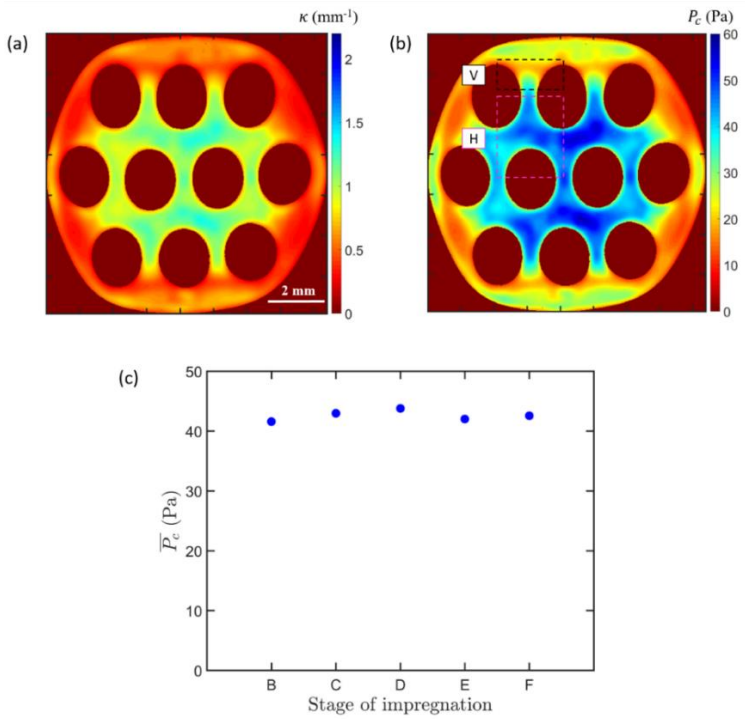

Figure 8. *(a) 2D map of the mean curvature κ of the fluid-air interface for stage B of the impregnation experiment performed using silicone oil. (b) Corresponding 2D map of the capillary pressure P_c. The traces of the tubes are not perfectly circular in the 2D maps because of their possible slight vertical misalignment. (c) Average capillary pressure $\overline{P_c}$ in the centre of the fibre network as a function of the impregnation stage.*

4. Discussion

4.1 Variations in the local contact angles

For both investigated fluids, this study revealed that during the impregnation experiments the local contact angles exhibited large variations along the triple lines formed onto the surfaces of the tubes. These observations were done during the wetting (upward motion of the fluid reservoir) or dewetting (downward motion of the fluid reservoir) of the fibre network with both fluids. This phenomenon was even more pronounced for the outer tubes of the network (Figure 3).

Similar observations using 3D images have already been made for geomaterials and granular materials with complex porous structures [31] [44] [45] [46] impregnated by a wetting fluid. If the wetting fluid is at rest (in "static" conditions), the variations of the local contact angle can be associated to several factors such as the local roughness and heterogeneities in the physico-chemical properties of the surface of solid, or the topology of pores [47]. A relaxation phenomenon of the local contact angles towards a stable equilibrium contact can also be a possible origin of these variations. Indeed, the authors observed that relaxation can occur at different rates along the contact lines and thus also leads to contact angle distributions.

Several authors [31] [44] have also reported that imbibition or drainage (fluid in "dynamic conditions) of a granular porous medium by a wetting phase can induce localised small

pressure perturbations in the wetting phase and variations in the contact angles. During imbibition, the authors observed motions of the contact lines once the contact angles approached (or exceeded) a maximal contact angle (denoted as the advancing contact angle). During drainage, they observed motions of the contact lines once the contact angles approached a minimum angle (denoted as the receding contact angle). Similar scenarios are expected to occur in our experiments and could explain why the triple lines were like anchored during the withdrawing of the reservoir (Figure 3).

4.2 Mesoscale capillary pressure measurements and theoretical predictions

From the local capillary pressure maps, we identified two characteristic zones (denoted H and V in Figure 8a,b) in order to estimate their mean capillary pressure $\bar{P}_c$. These zones were located in the centre and on the side of the fibre network, respectively. They corresponded to fluid-air interface zones that were nearly perpendicular (H) or parallel (V) to the tubes' axes. As mentioned previously in section 2.3.5, the algorithm proposed by Flin *et al.* [40][41] enables local unit normal vectors $\boldsymbol{n}$ to the fluid-air interface to be computed. The components of the average unit normal vector $\bar{\boldsymbol{n}}$ were (0.05, -0.13, -0.99) in zone H and (-0.01, -0.94, -0.34) in zone V, showing that these vectors were nearly aligned with the tube axes or perpendicular to the tube axes, respectively. Then, the average capillary pressure $\bar{P}_c$ was estimated in the fluid domain of zones H and V. In zone H (resp. V), the pressure $\bar{P}_c$ was equal to 45 Pa (resp. 21 Pa). The pressure measured in zone H is in accordance with that given by the fluid statics that can be estimated from the relative height $\bar{z}$ of the fluid-air interface and the gravity force g, i.e., $\bar{P} = \rho g \bar{z} \approx 39$ Pa. This shows once again that the mean curvature of the fluid-air interface is relevant. Then, we compared these values to the predictions of the model proposed by Ahn et al. [48] for the average capillary pressure $\bar{P}_c$ within arrays of parallel fibres:

$$\bar{P}_c = F \frac{\gamma_{lv} \cos\bar{\theta}\,(1-\phi_p)}{2\phi_p r_e} \tag{5}$$

where ϕ_p is the porosity, and F is a form factor that depends on the flow direction and fibre network geometry. For flow parallel or transverse to fibres, F is equal to 4 and 2, respectively [48]. To estimate the average capillary pressure $\bar{P}_c$ from Eq. 5, the average of the local contact angles was calculated along the portions of the triple lines formed along the tubes comprised in zones H or V (Figure 8b). For zone H, this average value $\bar{\theta}$ was equal to 35°, whereas for zone V it was equal to 28°. Furthermore, the porosity ϕ_p= 0.55 corresponds to the porosity of a period of the triangular tube arrangements that constitute the fibre network. Then, the model prediction for the average capillary pressure $\bar{P}_c$ was 38 Pa for zone H and 20 Pa for zone V, showing a good agreement with the experimental measurements.

4.3 Interest of measurements of capillary forces

The measurements of the pore scale capillary pressure and forces exerted by the fluid on the tubes performed in this study are original since they are entirely based on local geometric descriptors obtained from the quantitative analysis of 3D X-ray microtomography images.

The results gathered for the capillary pressure could be extended and down-scaled to industrial fibre bundles with similar porosity (ϕ_p= 0.55) and fibre arrangement but made of glass fibres with a smaller diameter (i.e., $2r_e$ = 15 µm). In that case, the capillary pressure would be one hundred times higher. However, contrary to what is observed in this study for the rigid fibre network, capillary-driven flows would be also coupled to (de)-consolidation phenomena characterised by complex re-arrangements and bending mechanisms of the fibres (see Figure 3 shown in S1). These phenomena have been highlighted by Larson *et al.* [24] who observed important 3D fibre re-arrangements associated to variations in the fibre volume fraction during the longitudinal impregnation of an industrial fibre bundle.

The measurements shown in subsection 3.2.3 revealed that during the longitudinal impregnation of the model tube bundle, the transverse capillary forces $F_{\perp}^{*}$ measured on the outer tubes are important and of the same order of magnitude as the longitudinal capillary forces $F_{\parallel}^{*}$. In networks with similar geometry (similar fibre arrangement and fibre length L = 16 mm) made of 15µm diameter glass fibres, these forces would severely deform each fibre and probably pull them closer to each other in the form of a denser aggregate [49][50]. As a first estimate, assuming clamped-free boundary conditions and a fibre Young's modulus E of 70 GPa, the transverse capillary force $F_{\perp} \approx 2\pi r_e \gamma_{lv} cos\theta_s$ (Figure 6a) exerted by the fluid would induce a deflection $\delta = 32F_{\perp}L^3/3E\pi(2r_e)^4$ of the outer fibres of the bundle equal to approx. 3 mm. This important deflexion induced by transverse capillary forces would then lead to complex re-arrangements of the fibres and to a (de)-consolidation (Figure 3 shown in S1) or a consolidation of the bundle.

This shows that the knowledge of such forces in real fibre bundles used for instance in composite processing routes such as pultrusion would help in properly controlling the fibrous microstructure of the obtained composite parts.

5. Conclusion

We carried out an analysis of capillary phenomena during the longitudinal impregnation of a fibre network made of arrays of parallel glass tubes that can be considered as cylindrical rods since the studied fluids cannot penetrate inside them during the experiments. For that purpose, a specific device was especially developed and allowed the acquisition of 3D X-ray microtomography images of several wetting and dewetting stages of the fibre network. Two types of wetting fluids, namely demineralised water and silicone oil, were used. Specific image analysis procedures were developed to measure the triple line lengths, local contact angles, and fluid-air interface mean curvatures. This original database allowed calculating the local capillary forces exerted on each tube of the fibre network by the fluid as well as the local capillary pressure. The results showed that the transverse forces may be as high as the longitudinal capillary forces. To the best of our knowledge, the measurements of the local transverse capillary forces exerted on the individual elements that constitute a fibre network are original. This is an important result for a better understanding and control of the impregnation phase of fibrous reinforcements used in composite materials because the propagation of a polymer matrix within industrial fibre bundles is partially governed by capillary forces that can often lead to complex rearrangement or deformation phenomena of

fibre bundles made of compliant fibres [49][50]. Our results confirmed that large variations in the local contact angles can occur in quasi static impregnation situations as it has already been reported in several studies dealing with the impregnation of geomaterials [31][44][45][46]. They also enabled assessing the relevance of the theoretical predictions proposed by Ahn et al. [48] for the upscaled capillary pressure. More particularly, the theroretical predictions for longitudinal and transverse flow situations were in accordance with our experimental measurements.

Finally, this study shows that a fine description of the geometry of the fluid-air interfaces, contact lines and local contact angles in fibre networks is accessible through the analysis of 3D images. It also shows that the local capillary pressure and forces can be finely estimated. It is also important to note that the numerical modelling of the presented results would certainly constitute a challenging task [51][52].

One limitation of this study is the important diameter of the tubes/fibres (approx. 1.5 mm) of the model fibre network compared to the typical diameter of fibres (approx. 10 to 300 µm) that are used in industrial fibre reinforcements of composite materials. However, thanks to recent progress offered by synchrotron radiation facilities (*e.g.*, voxel size smaller than 0.3^3 µm^3 and acquisition time smaller than 1s), the methodology proposed in this study could be extended to the study of capillary-driven flows occurring in industrial fibrous networks or fibre bundles that exhibit complex fibrous architectures (e.g. local variations of the fibre content, fibre misalignment). This experimental approach could also be extended to natural or synthetic fibrous networks made of deformable fibres. In these networks, impregnation phenomena are more complex than those observed in this study. To illustrate the relevance of the proposed approach to study elasto-capillary effects induced during impregnation, we have reported in Figure 3 shown in S1 a preliminary *in situ* longitudinal impregnation experiments that was carried out on a fibre bundle made of deformable PVDF fibres of diameter 160 µm and length 20 mm. The preliminary experiment shown in Figure 3 in S1 revealed severe distortion of the flow front with the formation of preferential flow channels and flow-induced (de)-consolidation of the deformable fibre bundle characterised by important re-arrangements and deformation mechanisms of the fibres. A finer analysis of impregnation mechanisms is in progress.

Acknowledgments – *C. Balbinot gratefully acknowledges the French Ministry of Higher Education and Research for her PhD research grant. The experiments were performed on beamline ID19 at the European Synchrotron Radiation Facility (ESRF) in the framework of the short proposal (MA-1498), Grenoble, France. The authors acknowledge the Paul Scherrer Institut (PSI), Villigen, Switzerland for provision of synchrotron radiation beamtime at beamline TOMCAT of the SLS and would like to thank Anne Bonnin for her assistance related to the experiments done on networks made of deformable PVDF fibres. The authors also thank H. Lakhdar-Chaouch (INSA Lyon) for her support in the experiments performed using the Krüss tensiometer and M. Terrien who helped design the impregnation device. The authors also endorse the research site of INSA Lyon at Oyonnax for administrative and technical support. The laboratories 3SR and LGP2 are parts of the LabEx Tec 21 (Investissements d'Avenir-grant agreement n◦ ANR-11-LABX-0030) and the Carnot Institute Polynat (n◦ ANR16-CARN-0025). CNRM/CEN is part of Labex OSUG@2020 (Investissements d'Avenir-grant agreement n◦ ANR-10-LABX-0056).*

References

[1] Advani SG, Hsiao K-T. Manufacturing techniques for polymer matrix composites (PMCs). Elsevier; 2012.

[2] Michaud V. A Review of Non-saturated Resin Flow in Liquid Composite Moulding processes. Transport in Porous Media 2016;115:581–601. https://doi.org/10.1007/s11242-016-0629-7.

[3] Park CH, Lee W. Modeling void formation and unsaturated flow in liquid composite molding processes: A survey and review. Journal of Reinforced Plastics and Composites 2011;30:957–77. https://doi.org/10.1177/0731684411411338.

[4] Chen Y -T, Davis HT, Macosko CW. Wetting of fiber mats for composites manufacturing: I. Visualization experiments. AIChE Journal 1995;41:2261–73. https://doi.org/10.1002/aic.690411009.

[5] Ruiz E, Achim V, Soukane S, Trochu F, Bréard J. Optimization of injection flow rate to minimize micro/macro-voids formation in resin transfer molded composites. Composites Science and Technology 2006;66:475–86. https://doi.org/10.1016/j.compscitech.2005.06.013.

[6] Caglar B, Tekin C, Karasu F, Michaud V. Assessment of capillary phenomena in liquid composite molding. Composites Part A: Applied Science and Manufacturing 2019;120:73–83. https://doi.org/10.1016/j.compositesa.2019.02.018.

[7] Binetruy C, Hilaire B, Pabiot J. Tow Impregnation Model and Void Formation Mechanisms during RTM. Journal of Composite Materials 1998;32:223–45. https://doi.org/10.1177/002199839803200302.

[8] Amico S, Lekakou C. Flow Through a Two-Scale Porosity , Oriented Fibre Porous Medium 2004:35–53.

[9] Schell JSU, Siegrist M, Ermanni P. Experimental determination of the transversal and longitudinal fibre bundle permeability. Applied Composite Materials 2007;14:117–28.

[10] Pillai KM, Advani SG. Wicking across a Fiber-Bank. Journal of Colloid and Interface Science 1996;110:100–10.

[11] Princen HM. Capillary phenomena in assemblies of parallel cylinders: II. Capillary rise in systems with more than two cylinders. Journal of Colloid and Interface Science 1969;30:359–71. https://doi.org/10.1016/0021-9797(69)90403-2.

[12] Neacsu V, Obaid AA, Advani SG. Spontaneous radial capillary impregnation across a bank of aligned micro-cylinders. Part II: Experimental investigations. International Journal of Multiphase Flow 2006;32:677–91. https://doi.org/10.1016/j.ijmultiphaseflow.2006.02.015.

[13] Bayramli E, Powell RL. Experimental investigation of the axial impregnation of oriented fiber bundles by capillary forces. Colloids and Surfaces 1991;56:83–100. https://doi.org/10.1016/0166-6622(91)80115-5.

[14] Yeager M, Simacek P, Advani SG. Role of fiber distribution and air evacuation time on capillary driven flow into fiber tows. Composites Part A: Applied Science and Manufacturing 2017;93:144–52. https://doi.org/10.1016/j.compositesa.2016.11.016.

[15] Qiu S, Fuentes CA, Zhang D, Van Vuure AW, Seveno D. Wettability of a Single Carbon Fiber. Langmuir 2016;32:9697–705. https://doi.org/10.1021/acs.langmuir.6b02072.

[16] Pucci MF, Liotier P-J, Drapier S. Capillary effects on flax fibers – Modification and characterization of the wetting dynamics. Composites Part A: Applied Science and Manufacturing 2015;77:257–65. https://doi.org/10.1016/j.compositesa.2015.03.010.

[17] Garat W, Pucci MF, Leger R, Govignon Q, Berthet F, Perrin D, et al. Surface energy determination of fibres for Liquid Composite Moulding processes: Method to estimate equilibrium contact angles from static and quasi-static data. Colloids and Surfaces A: Physicochemical and Engineering Aspects 2021;611:125787. https://doi.org/10.1016/j.colsurfa.2020.125787.

[18] Batch GL, Chen Y-T, Macoskot CW. Capillary Impregnation of Aligned Fibrous Beds: Experiments and Model. Journal of Reinforced Plastics and Composites 1996;15:1027–51. https://doi.org/10.1177/073168449601501004.

[19] Amico SC, Lekakou C. Axial impregnation of a fiber bundle. Part 1: Capillary experiments. Polymer Composites 2002;23:249–63. https://doi.org/10.1002/pc.10429.

[20] Neacsu V, Leisen J, Beckham HW, Advani SG. Use of magnetic resonance imaging to visualize impregnation across aligned cylinders due to capillary forces. Exp Fluids 2007;42:425–40. https://doi.org/10.1007/s00348-007-0251-0.

[21] Endruweit A, Glover P, Head K, Long AC. Mapping of the fluid distribution in impregnated reinforcement textiles using Magnetic Resonance Imaging: Application and discussion. Composites Part A: Applied Science and Manufacturing 2011;42:1369–79. https://doi.org/10.1016/j.compositesa.2011.05.020.

[22] Bréard J, Saouab A, Bouquet G. Dependence of the Reinforcement Anisotropy on a Three Dimensional Resin Flow Observed by X-Ray Radioscopy. Journal of Reinforced Plastics and Composites 1999;18:814–26. https://doi.org/10.1177/073168449901800903.

[23] Vilà J, Sket F, Wilde F, Requena G, González C, LLorca J. An in situ investigation of microscopic infusion and void transport during vacuum-assisted infiltration by means of X-ray computed tomography. Composites Science and Technology 2015;119:12–9. https://doi.org/10.1016/j.compscitech.2015.09.016.

[24] Larson NM, Zok FW. Insights from in-situ X-ray computed tomography during axial impregnation of unidirectional fiber beds. Composites Part A: Applied Science and Manufacturing 2018;107:124–34. https://doi.org/10.1016/j.compositesa.2017.12.024.

[25] Castro J, Sket F, González C. S-XCT experimental determination of local contact angle and meniscus shape in liquid moulding of composites. Composites Science and Technology 2020;199:108362. https://doi.org/10.1016/j.compscitech.2020.108362.

[26] Klise KA, Moriarty D, Yoon H, Karpyn Z. Automated contact angle estimation for three-dimensional X-ray microtomography data. Advances in Water Resources 2016;95:152–60. https://doi.org/10.1016/j.advwatres.2015.11.006.

[27] Scanziani A, Singh K, Blunt MJ, Guadagnini A. Journal of Colloid and Interface Science Automatic method for estimation of in situ effective contact angle from X-ray micro tomography images of two-phase flow in porous media 2017;496:51–9. https://doi.org/10.1016/j.jcis.2017.02.005.

[28] Alratrout A, Raeini AQ, Bijeljic B, Blunt MJ. Advances in Water Resources Automatic measurement of contact angle in pore-space images. Advances in Water Resources Journal 2017;109:158–69. https://doi.org/10.1016/j.advwatres.2017.07.018.

[29] Ibekwe A, Pokrajac D, Tanino Y. Computers and Geosciences Automated extraction of in situ contact angles from micro-computed tomography images of porous media. Computers and Geosciences 2020;137:104425. https://doi.org/10.1016/j.cageo.2020.104425.

[30] Armstrong RT, Porter ML, Wildenschild D. Linking pore-scale interfacial curvature to column-scale capillary pressure. Advances in Water Resources 2012;46:55–62. https://doi.org/10.1016/j.advwatres.2012.05.009.

[31] Andrew M, Menke H, Blunt MJ, Bijeljic B. The Imaging of Dynamic Multiphase Fluid Flow Using Synchrotron-Based X-ray Microtomography at Reservoir Conditions. Transport in Porous Media 2015;110. https://doi.org/10.1007/s11242-015-0553-2.

[32] Singh K. Imaging of oil layers, curvature and contact angle in a mixed- wet and a water-wet carbonate rock. Water Resources Research 2016:1–13. https://doi.org/10.1002/2015WR018072.Received.

[33] Lin Q, Bijeljic B, Pini R, Blunt MJ, Krevor S. Imaging and Measurement of Pore-Scale Interfacial Curvature to Determine Capillary Pressure Simultaneously With Relative Permeability 2018:7046–60. https://doi.org/10.1029/2018WR023214.

[34] Latil P, Orgéas L, Geindreau C, Dumont PJJ, Rolland du Roscoat S. Towards the 3D in situ characterisation of deformation micro-mechanisms within a compressed bundle of fibres. Composites Science and Technology 2011;71:480–8. https://doi.org/10.1016/j.compscitech.2010.12.023.

[35] Laurencin T, Orgéas L, Dumont PJJ, Rolland du Roscoat S, Laure P, Le Corre S, et al. 3D real-time and in situ characterisation of fibre kinematics in dilute non-Newtonian fibre suspensions during confined and lubricated compression flow. Composites Science and Technology 2016;134:258–66. https://doi.org/10.1016/j.compscitech.2016.09.004.

[36] Paganin D, Mayo SC, Gureyev TE, Miller PR, Wilkins SW. Simultaneous phase and amplitude extraction from a single defocused image of a homogeneous object. Journal of Microscopy 2002;206:33–40. https://doi.org/10.1046/j.1365-2818.2002.01010.x.

[37] Krasnoshlyk V, Rolland du Roscoat S, Dumont PJJ, Isaksson P, Ando E, Bonnin A. Three-dimensional visualization and quantification of the fracture mechanisms in sparse fibre networks using multiscale X-ray microtomography. Proceedings of the Royal Society A: Mathematical, Physical and Engineering Sciences 2018;474:20180175. https://doi.org/10.1098/rspa.2018.0175.

[38] Schneider CA, Rasband WS, Eliceiri KW. NIH Image to ImageJ: 25 years of image analysis. Nature Methods 2012;9:671–5. https://doi.org/10.1038/nmeth.2089.

[39] James DF. The meniscus on the outside of a small circular cylinder. Journal of Fluid Mechanics 1974;63:657–64. https://doi.org/10.1017/S0022112074002126.

[40] Flin F, Brzoska JB, Lesaffre B, Coléou C, Pieritz RA. Three-dimensional geometric measurements of snow microstructural evolution under isothermal conditions. Annals of Glaciology 2004;38:39–44. https://doi.org/10.3189/172756404781814942.

[41] Flin F, Brzoska JB, Coeurjolly D, Pieritz RA, Lesaffre B, Coléou C, et al. Adaptive estimation of normals and surface area for discrete 3-D objects: Application to snow binary data from X-ray tomography. IEEE Transactions on Image Processing 2005;14:585–96. https://doi.org/10.1109/TIP.2005.846021.

[42] Molnár G, Ganster P, Török J, Tanguy A. Sodium effect on static mechanical behavior of MD-modeled sodium silicate glasses. Journal of Non-Crystalline Solids 2016;440:12–25. https://doi.org/10.1016/j.jnoncrysol.2016.02.024.

[43] Henderson MA. The interaction of water with solid surfaces: fundamental aspects revisited. Surface Science Reports 2002;46:1–308. https://doi.org/10.1016/S0167-5729(01)00020-6.

[44] Andrew M, Bijeljic B, Blunt MJ. Pore-scale contact angle measurements at reservoir conditions using X-ray microtomography. Advances in Water Resources 2014;68:24–31. https://doi.org/10.1016/j.advwatres.2014.02.014.

[45] Alhosani A, Lin Q, Scanziani A, Andrews E, Zhang K, Bijeljic B, et al. Pore-scale characterization of carbon dioxide storage at immiscible and near-miscible conditions in altered-wettability reservoir rocks. International Journal of Greenhouse Gas Control 2021;105:103232. https://doi.org/10.1016/j.ijggc.2020.103232.

[46] Ibekwe A, Pokrajac D, Tanino Y. Automated extraction of in situ contact angles from micro-computed tomography images of porous media. Computers & Geosciences 2020;137:104425. https://doi.org/10.1016/j.cageo.2020.104425.

[47] AlRatrout A, Blunt MJ, Bijeljic B. Spatial Correlation of Contact Angle and Curvature in Pore-Space Images. Water Resources Research 2018;54:6133–52. https://doi.org/10.1029/2017WR022124.

[48] Ahn KJ, Seferis JC, Berg JC. Simultaneous measurements of permeability and capillary pressure of thermosetting matrices in woven fabric reinforcements. Polymer Composites 1991;12:146–52. https://doi.org/10.1002/pc.750120303.

[49] Duprat C, Protière S, Beebe AY, Stone HA. Wetting of flexible fibre arrays. Nature 2012;482:510–3. https://doi.org/10.1038/nature10779.

[50] Bico J, Roman B, Moulin L, Boudaoud A. Elastocapillary coalescence in wet hair. Nature 2004;432:690–690. https://doi.org/10.1038/432690a.

[51] Charpentier J-B, Brändle de Motta JC, Ménard T. Capillary phenomena in assemblies of parallel cylindrical fibers: From statics to dynamics. International Journal of Multiphase Flow 2020;129:103304. https://doi.org/10.1016/j.ijmultiphaseflow.2020.103304.

[52] Chevalier L, Bruchon J, Moulin N, Liotier P-J, Drapier S. Accounting for local capillary effects in two-phase flows with relaxed surface tension formulation in enriched finite elements. Comptes Rendus Mécanique 2018;346:617–33. https://doi.org/10.1016/j.crme.2018.06.008.